# Highly flexible, mechanically strengthened metallic glass-based composite electrode with enhanced capacitance and cyclic stability

Xu, Yi; Yiu, Pak Man; Wang, Yu-Kun; Qin, Xiao-Meng; Shibayama, Tamaki; Watanabe, Seiichi; Ohnuma, Masato; Chen, Da-Zhu; Cheng, Hua; Shek, Chan-Hung; Lu, Zhou-Guang; Liu, Chen

**Published in:**
Rare Metals

**Published: 01/11/2022**

**Document Version:**
Post-print, also known as Accepted Author Manuscript, Peer-reviewed or Author Final version

**Publication record in CityU Scholars:**
Go to record

**Published version (DOI):**
10.1007/s12598-022-02060-8

**Publication details:**
Xu, Y., Yiu, P. M., Wang, Y.-K., Qin, X.-M., Shibayama, T., Watanabe, S., Ohnuma, M., Chen, D.-Z., Cheng, H., Shek, C.-H., Lu, Z.-G., & Liu, C. (2022). Highly flexible, mechanically strengthened metallic glass-based composite electrode with enhanced capacitance and cyclic stability. *Rare Metals*, *41*(11), 3717–3728. https://doi.org/10.1007/s12598-022-02060-8

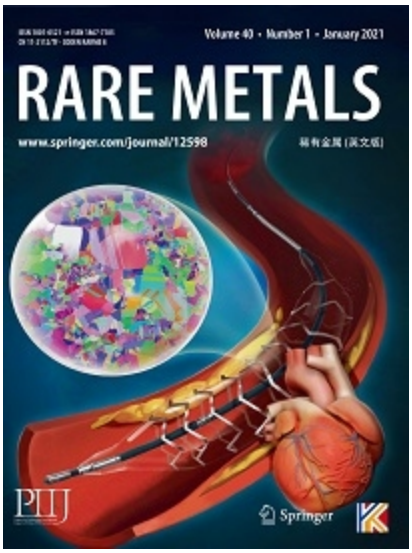


# Highly flexible, mechanically strengthened metallic glass-based composite electrode with enhanced capacitance and cyclic stability

| | |
|---|---|
| Journal: | *Rare Metals* |
| Manuscript ID | RMET-0921-0548.R1 |
| Manuscript Type: | Original Article |
| Date Submitted by the Author: | 17-Nov-2021 |
| Complete List of Authors: | Xu, Yi; Shenzhen University, college of Materials Science and Engineering<br>Yiu, Pak Man; City University of Hong Kong, Department of Materials Science and Engineering<br>Wang, Yu-Kun; City University of Hong Kong, Department of Materials Science and Engineering<br>Qin, Xiao-Meng; City University of Hong Kong, Department of Materials Science and Engineering<br>Shibayama, Tamaki; Hokkaido University, Faculty of Engineering<br>Watanabe, Seiichi; Hokkaido University, Faculty of Engineering<br>Ohnuma, Masato; Hokkaido University, Faculty of Engineering<br>Chen, Da-Zhu; Shenzhen University, College of Materials and Engineering<br>Cheng, Hua; Southern University of Science and Technology, Department of Materials Science and Engineering<br>Shek, Chan-Hung; City University of Hong Kong, Department of Materials Science and Engineering<br>Lu, Zhuguang; Southern University of Science and Technology, Department of Materials Science and Engineering<br>Liu, Chen; Shenzhen University, College of Materials and Engineering |
| Keywords: | Metal-matrix composites (MMCs), Thin films, Porosity, Nano-structures |
| Speciality: | Supercapacitors < Energy Storage |

# Highly flexible, mechanically strengthened metallic glass-based composite electrode with enhanced capacitance and cyclic stability

Yi Xu[a,b], Pak Man Yiu[d], Yu-Kun Wang[d], Xiao-Meng Qin[d], Tamaki Shibayama[e], Seiichi Watanabe[e], Masato Ohnuma[e], Da-Zhu Chen[a], Hua Cheng[c], Chan-Hung Shek*[d], Zhouguang Lu*[c], Chen Liu*[a]

a. Guangdong Research Center for Interfacial Engineering of Functional Materials, College of Materials Science and Engineering, Shenzhen University, Shenzhen 518060, PR China

b. College of Physics and Optoelectronic Engineering, Shenzhen University, Shenzhen.

c. Guangdong-Hong Kong-Macao Joint Laboratory for Photonic-Thermal-Electrical Energy Materials and Devices, Department of Materials Science and Engineering, Southern University of Science and Technology, Shenzhen 518060, PR China

d. Department of Materials Science and Engineering, City University of Hong Kong, No.83 Tat Chee Avenue, Kowloon Tang, Hong Kong, China

e. Centre for Advanced Research of Energy and Materials, Division of Quantum Science and Engineering, Faculty of Engineering, Hokkaido University, Kita 13, Nishi 8, Kita Ku, Sapporo 0608628, Japan

* Email address: liuchen@szu.edu.cn (C. Liu), luzg@sustech.edu.cn (Z. G. Lu), apchshek@cityu.edu.hk (C.H.Shek)

**ABSTRACT** The design of flexible composite electrodes has become the top priority in energy storage devices for the development of future wearable intelligent electronics. However, searching for fully integrated, ultrathin flexible composite electrodes with satisfying electrochemical performance is still a major challenge. Herein, we introduce a nanoporous gold metallic glass (MG) ribbon based composite electrode with excellent electric conductivity, mechanical flexibility, and extra capacitance by integrating PPy into wrinkled nanoporous ribbon (NPG@MG). The "freestanding, ultrathin, highly conductive and flexible" nature of the composite electrode prevents the conducting polymer from structural instability resulting from the volume swell and shrink during the charging/discharging circulation and the packed PPy provides protection for the wrinkled topology on the surface of the MG ribbon. The capacitance of pure NPG@MG-PPy composite electrode reached 393 mF $cm^{-2}$. The ultra-thin all-solid-state flexible supercapacitor demonstrates an excellent capacitance of 172 mF $cm^{-2}$ (14.8 F $cm^{-3}$), accompanied by a superior cycling capability after 8000 charge/ discharge cycles attributed to mechanical flexibility. The areal energy density also reached 0.74 mWh $cm^{-3}$ (9 μWh $cm^{-2}$) at a power density of 1 μW $cm^{-2}$. This work provides valuable concepts on the design of PPy-based hybrid materials for flexible energy storage systems with greatly enhanced electrochemical performances.

**Keywords:** Metal-matrix composites (MMCs), Thin films, Porosity, Nano-structures.

## 1. Introduction

The design of flexible energy storage devices has been an impending challenge for the future development and application of wearable intelligent electronics. Among various supporting power sources for such portable electronic systems, supercapacitors have been achieved more attention owing to their merits of fast charge and discharge rate, high power density and easy processability. However, the lower energy density compared with alkaline batteries inhibits the further development of supercapacitor. [1,2] Commercially available supercapacitor can provide energy densities of limited to 10 Wh $kg^{-1}$ compared with batteries (30-40 Wh $kg^{-1}$). In addition, nanoprous (activated) carbon based electrodes have been mostly discussed that the capacitance is limited to 30–50 Wh/kg for organic electrolyte and to 12–17 Wh/kg for aqueous electrolyte. Furthermore, the assembled protype symmetric supercapacitor cell fabricated nanoporous(activated) carbon is reached lower than 10 Wh/kg. To meet the trend of portable device and solve low energy density issue, an energy storage system having flexible electrodes with satisfying electrochemical performance has become the top priority.

A flexible and conductive substrate that can be utilized as a current collector is one of the core components for flexible energy storage systems. The porous substrates (polymer films and textile fabric) have long been thought to be suitable substrates because of their low cost and flexibility that can bind active electrode materials. [3–7] However, their insulating nature makes them have to be treated with electrically conductive materials (e.g. carbon nanotubes, metallic particles). The nanoporous metal (NPM) with three-dimensional bi-continuous ligaments and excellent electrical conductivity are conductive to

be applied as the substrate for fabricating composite electrode. [8–11] The high-volume fraction of pores in NPM substrate could provide fast ion conduction through loading different active materials. This gives rise to the good ion and electron transportation by the interaction of active materials with the substrate ligaments, which would contribute to the greatly enhanced electrochemical performance at high charge/discharge rates. Even so, most of the NPM structures exhibit a fatal weakness of frangibility and the totally dealloyed materials break easily into the pieces. However, the amorphous dealloying metallic glass (MG) ribbons without crystalline defects enable them with high mechanical strength, which is very suitable for using as electrode substrate but has long been neglected. [12,13]

Additionally, many studies on energy density improvement through the use of pseudocapacitive electrode materials such as metal oxides or electrochemically active molecules/polymers have been reported. (14–18) Thereinto, metal oxides ($MnO_2$ ,$RuO_2$, $Fe_2O_3$, NiO, $NiCo_2O_4$) are commonly introduced onto an electrically conductive substrate via hydrothermal reaction or chemical deposition. (19–26) However, the low active materials loading in the electrodes caused by the low porosity, unsatisfactory mechanical bending resistance and poor electrical conductivity of the textile substrates, which severely limits the applications of flexible electrodes. Conducting polymer Polypyrrole (PPy) has been widely used as pseudocapacitive electrode materials to fabricate flexible supercapacitors due to its intrinsic flexibility and conductivity. (27–36) However, the poor cycling performance caused by the structural instability through reduplicative volumetric expansion and contraction during charge and discharge processes, respectively. (37–39) In addition, the dense structure of freestanding PPy film generated in electrochemical

polymerization process only has limited capacitance. (17,36) Searching for a versatile substrate to deal with the above issues have become a crucial challenge for the development of flexible supercapacitors.

Herein we demonstrate a nanoporous gold (NPG) structure with continuous wrinkled topology and flexible MG interlayer by a facile dealloying process. Owing to the excellent mechanical flexibility and electric conductivity of MG ribbon, the wrinkled nano-porous Au-based MG ribbon (denoted as NPG@MG hereafter) can be taken as ideal substrate and current collector for electrochemically depositing polypyrrole into the nanopores. Combing the merits of metallic glass and conducting polymer materials, the capacitance of the as-fabricated freestanding NPG@MG-PPy electrode reached 393 mF $cm^{-2}$, which is 2.6 times greater than pristine PPy film. The all-solid-state supercapacitors exhibit cyclic stability with no capacitance loss after 8000 charging and discharging cycles. In addition, the all-solid-state supercapacitor also exhibited excellent capacitance retention even under repeatedly bending and coiling without any performance degradation, indicating the superb cycling stability and deformation prevention. Our strategy offers a new route to enhance the capacitance and cyclic performance of ultrathin and bendable supercapacitors for wearable and portable electronic systems.

## 2. Results and discussion

### 2.1. Design of Flexible Supercapacitor

Our design strategy is schematically illustrated in Fig. 1. The as-spun strong and flexible $Au_{55}Cu_{25}Si_{20}$ MG ribbon was cleaned and then dealloyed in iron chloride solution. After dealloying, a notable bi-continuous nanoporous structure with specific cone-shaped protrusion emerged on the top surface of the Au-based MG ribbon that formed wrinkled topology (Fig. 1e). As a result, distinct continuous wrinkles were formed by the uplifted mound-shaped projections overlapping with each other on the top of the flexible MG interlayer. This specific phenomenon could sharply increase the surface areas and density of active sites. The NPG structure on the ribbon surface could serve as electrochemically active sites to provide a coarse morphology favouring the PPy electro-polymerization process. With the assistance of these ligaments and protrusions, an adequate amount of PPy could be simply deposited and wrapped on the surface. In addition, the PPy film wrapped on the top surface provided an elastic support and protect the ligaments from deformation. Moreover, the Au-based MG ribbon could be tailored into different sizes, including the very narrow width of 1 mm (Fig. 1f), which is essential to applications for flexible and portable electronic devices as well as wearable and knittable devices in various working conditions. We also fabricated and measure the performance of flexible solid-state supercapacitor in practical conditions, in which a PVA gel electrolyte serving as a separator was sandwiched by two identical pieces of NPG@MG-PPy electrodes. This length scale fits the need for small-scale energy storage system of the future light weight and portable electronic device. Since the dealloyed ribbon inherited the high elasticity and good

mechanical flexibility of Au-based MG ribbon due to the ductile MG interlayer, the fabricated all-solid-state energy storage device could therefore be freely bent. In consideration of the outstanding electrical conductivity and mechanical behavior, the Au-based MG could be prepared as an ideal current collector for a flexible supercapacitor. Fig.1g shows the all-solid-state flexible supercapacitor formed by the application of dealloyed Au-based MG ribbon with PPy deposition.

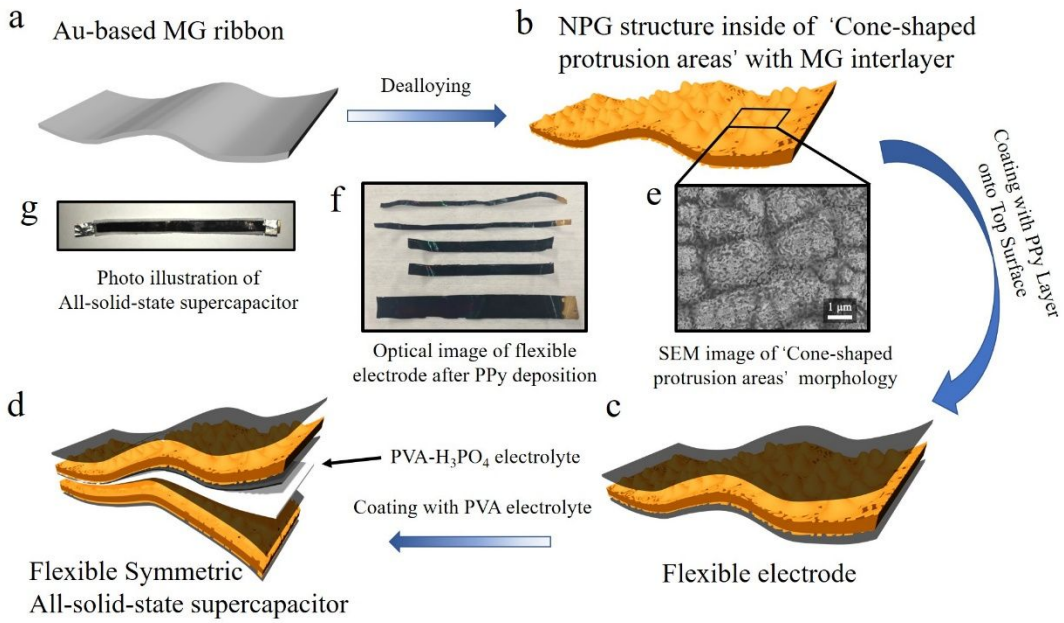


**Fig. 1** (a) Schematic illustration of the Au-based MG ribbon and (b) nanoporous gold structure after dealloying process. (c) Schematic illustration for the fabrication of flexible electrode and (d) subsequently symmetric all-solid-state supercapacitor. (e) SEM image of electrochemical polymerization of PPy on NPG structure. (f) Image of the freestanding @MG-PPy as electrode, and (g) function as flexible all-solid-state supercapacitor.

### 2.2. Structural and morphological characterization

The formation process of NPG@MG-PPy structure was firstly studied with SEM. The

as-spun metallic glass ribbon had a smooth surface (Fig. 2a). The surface roughness increased and a 3D bicontinuous pore/ligament network in nanoscale was observed in the cone-shaped projection after dealloying (Fig. 2b). The inherent cone-shaped protrusion formation mechanism had been discussed in detail in our previous study. [38] The density and thickness of cone-shaped protrusions areas could be controlled by adjusting the dealloying process parameters. In order to obtain the optimum performance, the dealloying time and temperature were set as 20 minutes and 70 °C, respectively. It was observed a notable PPy film covered on the ligaments after a 10 s electro-polymerization of PPy onto the NPG surface (Fig. 2c). The XRD pattern of NPG@MG without PPy deposition exhibit the typical FCC phase for pure metallic gold as shown in Fig.S3a. As the PPy film formed, the XRD peak located at around 27° corresponded to the PPy chains, which is overlapped with the broad amorphous hump, as seen in the XRD pattern (Fig. S3b).

As the electrochemical polymerization time increased to 20 s, the PPy layer homogeneously covered the surface and the thickness of the PPy film increased to 50nm, (Fig. 2d). Excessive deposition of PPy deteriorated electrochemical performance. The bicontinuous ligaments, which were directly connected to MG interlayer, were rather conductive to avoid excess charge accumulation issue. It is clear that the ligaments' structure was gradually concealed when the electrochemical polymerization time was increased to 40s. The coating was still thin enough to allow a fast capacitance response and avoided channel congestion. After deposition for 60 s, the NPG surface morphology were totally shielded and the PPy accumulation bumps appeared. Such morphological development during the polymerization process would significantly affect the

electrochemical behavior of the assembled supercapacitors.

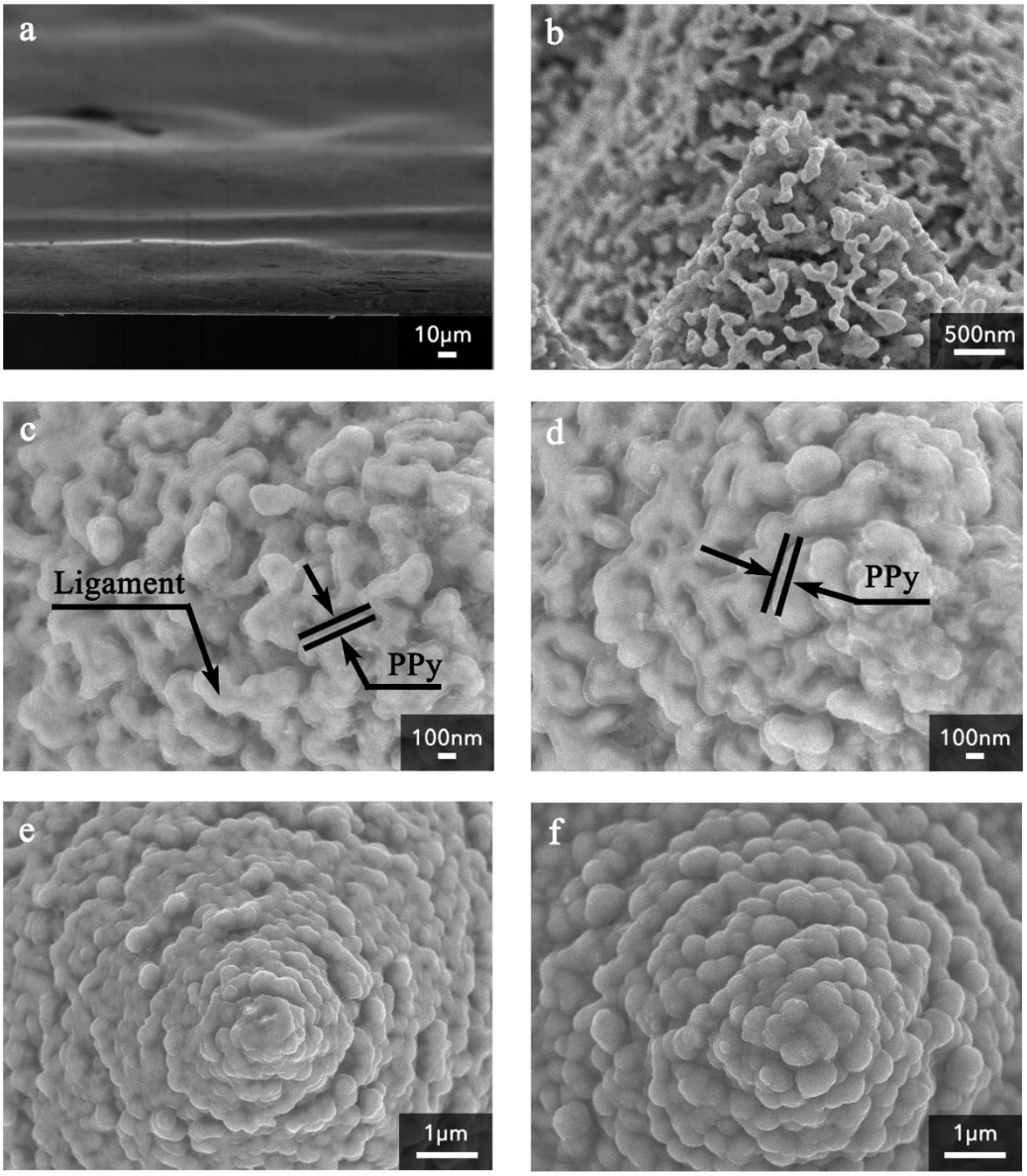


**Fig. 2** SEM image of Au-based MG ribbon (a)before and (b)after dealloying process. SEM image after electrochemically polymerizing PPy for (c) 10, (d) 20, (e) 40 and (f) 60 s.

The formation of the porous structure was briefly described in the following based on transmission electron microscopy (TEM) images of samples obtained in the cone-shaped protrusion region by focused ion beam (FIB). Bicoutinuous ligaments and pores were

present in the top region of the cone-shaped protrusion (Fig. 3a). The average pore size was ~ 5 nm in the initial dealloying stage (Fig. 3b). As the dealloying proceeded, the pore size gradually increased to 100 nm (Fig. 3c-d). The depletion of copper atoms in the initial dealloyed sites resulted in transformation from amorphous state to gold silicide phase. Owing to the instability of gold silicide and tendency of lowering the surface energy, the metastable gold silicide decomposed into gold nanoparticles and the silicon diffused to the surface and oxidized into SiOx (Fig. 3e-f), which is in agreement with the observation shown in HAADF-STEM image with composition x-ray mapping of Au-La, Cu-La, Si-La lines, respectively. It also demonstrated the dissolution of copper atoms and surface diffusion of silicon atoms. After initial dealloying stage, XRD patterns displayed a broad curve without any sharp peak in the range of 15-25°, indicating a typical amorphous structure of the Au-based MG ribbon (Fig. S2). After dealloying for 20 min, the diffraction peaks centered at 38.2°, 44.4°, 64.6°, 77.6° and 81.7° correspond to the pure metallic gold phase structure (JCPDS, card No. 04-0784), indicating the appearance of gold particles. The decomposition of gold silicide led to the enlargement of pore size and increase of ligament diameter. Meanwhile, the formation of nanopores during initial dealloying close to the MG and ligaments interface (Fig. S1) was occurring simultaneously. Thus, the internal strain generated during both dealloying stages lead to the formation of cone-shaped protrusion.

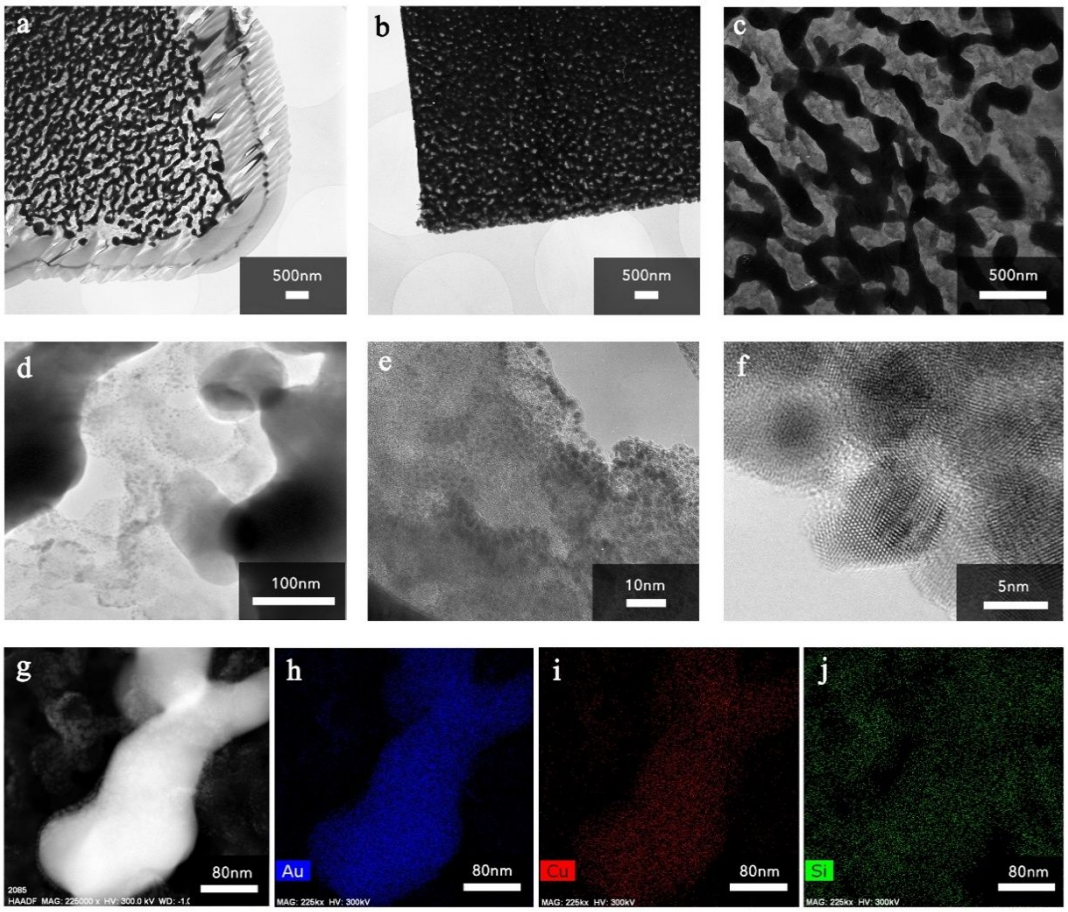


**Fig. 3** (a,b) HRTEM image of 'cone shape' areas and (c,d) nanoporosity areas. (e,f) Enlarged HRTEM image of gold nanoparticles formed on the surface of ligament and (g) HAADF-STEM images of ligaments and (h–j) EDS elemental mapping of (h) Au, (i) Cu and (j) Si.

The large spacing between the ligaments and the rough morphology was favourable for the deposition of PPy film onto NPG surface. The gold nanoparticles on the top of the ligaments could be regarded as active sites. The cone-shaped protrusions, bi-continuous ligaments and pores inside the structure provided a larger specific surface area that could enhance the capacitance of the fabricated electrode materials. In Fig. 4a, the formation of PPy film was confirmed by X-ray photoelectron spectroscopy (XPS) techniques. In Fig.

S4b, the core level spectra of C1s for the NPG@MG-PPy film sample could be fitted into three Gaussian peaks. The peak located at 285.1 eV correspond to C-N bonds (α carbon) of pyrrole, while the peak locates at 284.4 eV and 286.2 eV correspond to C-C bonds (β carbons) and C-O bonds (carbonyl carbons), respectively. In Fig. S4c, the core level of N1s spectra could be divided into three Gaussian peaks. The peaks located at 399.6, 401.5, and 402.5 eV attributed to the neutral secondary amine nitrogen (-NH-), the protonation benzenoid amine (-N+H-) and protonation quinonoid imine (=N+H-) structures, respectively.

**2.3. The electrochemical characterization of NPG@MG-PPy electrode**

Fig. 4a shows the cyclic voltammetry (CV) profiles determined at various scan rates (starting from 5 $mVs^{-1}$ to 500 $mVs^{-1}$). The maintained rectangular shapes of the CV curves measured even at a high scan rate of 500 mV $s^{-1}$ indicated the low resistance of the freestanding NPG@MG-PPy electrode and good reversible process during the charging /discharging circulation. Fig. 4b shows the CV curves of the electrodes with PPy electro-polymerization time increasing from 10 to 60 s at scan rate of 200 mV/s. It is obvious that current density increased dramatically when increasing the time of PPy electro-polymerization from 10s to 40s, suggesting the increased charge storage capacity with thicker PPy layer deposited onto the NPG. However, the CV profile of the electrode with 60s PPy deposition remains the same shape as that of 40s, which suggests that excess accumulation of PPy deteriorates the electron conductivity. Fig. S5 shows the detailed CV profile of the various PPy electrodes measured at different scan rates, which exhibits the capacitance enhancement stalled after 60s electro-polymerization time. Therefore, the optimal electro-polymerization time of PPy on NPG structure was determined as 40 s.

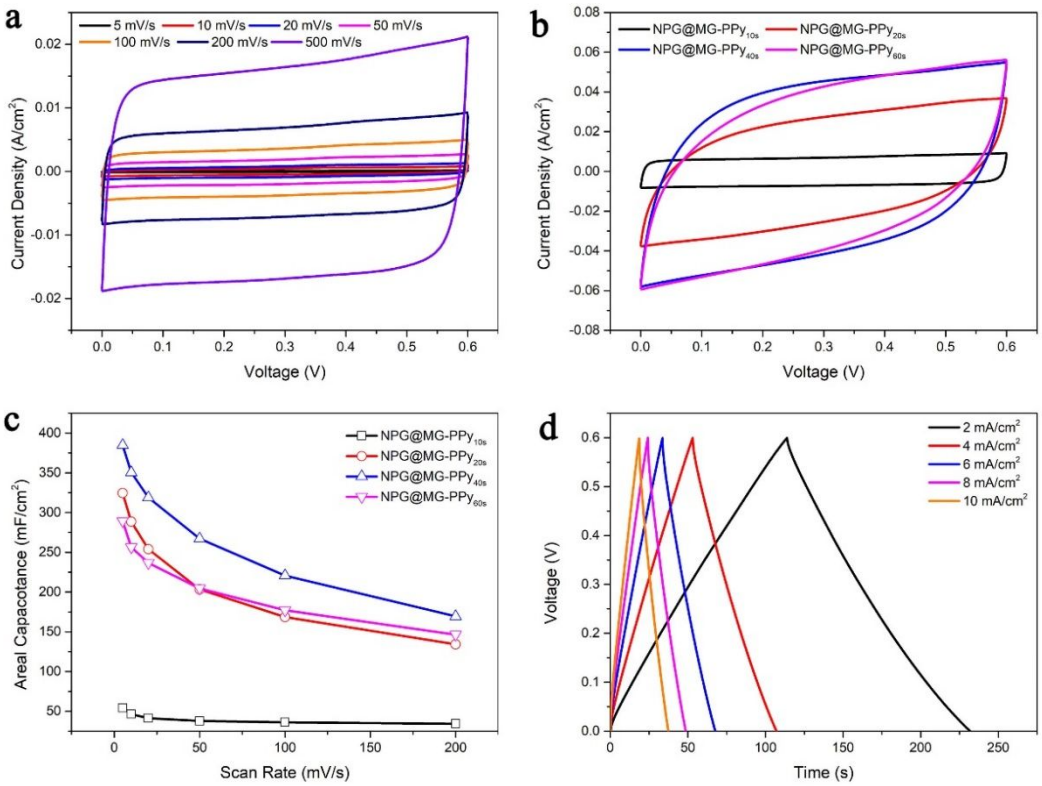


**Fig. 4** (a) CV curves of the $PPy_{10s}$ film deposited on NPG morphology at various scan rates. (b) CV curves of the $PPy_{10s}$, $PPy_{20s}$, $PPy_{40s}$ and $PPy_{60s}$ film deposited on NPG at 200 mV $s^{-1}$. (c) Areal capacitances as functions of scan rates with various electrodeposition times. (d) Galvanostatic charging/discharging curves of $PPy_{40s}$ film deposited on NPG at various current density.

Fig. 4c shows the areal capacitances of electrode samples measured at various scan rates. The capacitances notably enhanced with the increasing deposition time until 40s. In addition, the decay rate ability of areal capacitance calculated from CV curves reveals over 50% retention even the scan rates increasing to 200 mV/s. However, the decay of capacitances with respect to the scan rate for the 40s electro-polymerization was lower than that of 60 s. These indicates that excessive accumulation of PPy hindered electron

transportation and ion accessibility, which agrees to the discussions above. Fig. 4d exhibits galvanostatic charging/discharging (GCD) behaviors of $PPy_{40s}$ freestanding electrode at specific currents of 2, 4, 6, 8 and 10 mA/cm$^2$, respectively. The nearly triangular shaped of GCD curves measured at different current densities further demonstrated the high reversible process during the charging/discharging circulation and good columbic efficiency of the $PPy_{40s}$ electrode. As calculated from the GCD curves in Fig. 4d and S6, the areal capacitance of the freestanding $PPy_{40s}$ electrode at 10 mA cm$^{-2}$ still remained at above 79% (393–311 mF cm$^{-2}$) compared to that of low current density of 2 mA cm$^{-2}$, which was more than 2.6 times than that of the pristine PPy film (150 mF cm$^{-2}$). The satisfactory performance of PPy-based electrode could endure fast voltage and current change rates, which was believed to be a result of effective electrochemical dynamic processes in the supercapacitor devices structure.

### 2.4. Electrochemical Properties of NPG@MG-PPy Based All-Solid-State Flexible Supercapacitor

Freestanding NPG@MG-$PPy_{40s}$ hybrid electrode exhibited excellent flexibility and electrochemical performance arising from PPy film integrated into the surface ‘cone shaped protrusion’ NPG structure. It could be functioned as an excellent ultra-thin electrode to fabricate flexible all-solid-state supercapacitors. Fig. 5a demonstrates the fabricated all-solid-state supercapacitor taking advantage of the NPG@MG-$PPy_{40s}$ as the electrode. The excellent flexibility attributed to the synergy effect of PPy film and Au-based MG ribbon allowed the as-prepared all-solid-state supercapacitor to be bent to almost 180° without breaking. The thickness of the entire device is measured to be as thin as 117 μm

(Fig. 5b). With the effect of PPy film deposited on NPG, the area of the enclosed CV curves is obviously much larger than that of the pure NPG all-solid-state supercapacitor (Fig. 5c). It indicated the increased capacitance and good reversibility during the charging and discharging process after the PPy film was introduced. The capacitance of the entire device was 172 mF $cm^{-2}$ (14.8 F $cm^{-3}$), which was 23% higher than that of solid-state supercapacitor with pure NPG electrode and two orders of magnitude higher than those of previous PPy-based Supercapacitor, as calculated from the GCD curves at a current density of 0.2 mA $cm^{-2}$ (Fig. 5d). In addition, the capacitance of supercapacitor with pure NPG electrode dropped sharply and only retain 56% capacity as the current density increased to 1 mA $cm^{-2}$, while the NPG@MG-$PPy_{40s}$ supercapacitor still retained 91.8% capacity (Fig. 5d). It was worth noting that the CV curves of NPG@MG-$PPy_{40s}$ supercapacitor kept good rectangular shape (Fig. 5e) within a selected range of potential even at a high scan rates of 500 mV $s^{-1}$. This feature indicated the fast diffusion of ions in the electrodes and that the entire device showed a more rapid current response to voltage reversal than the standalone NPG@MG-$PPy_{40s}$ electrode.

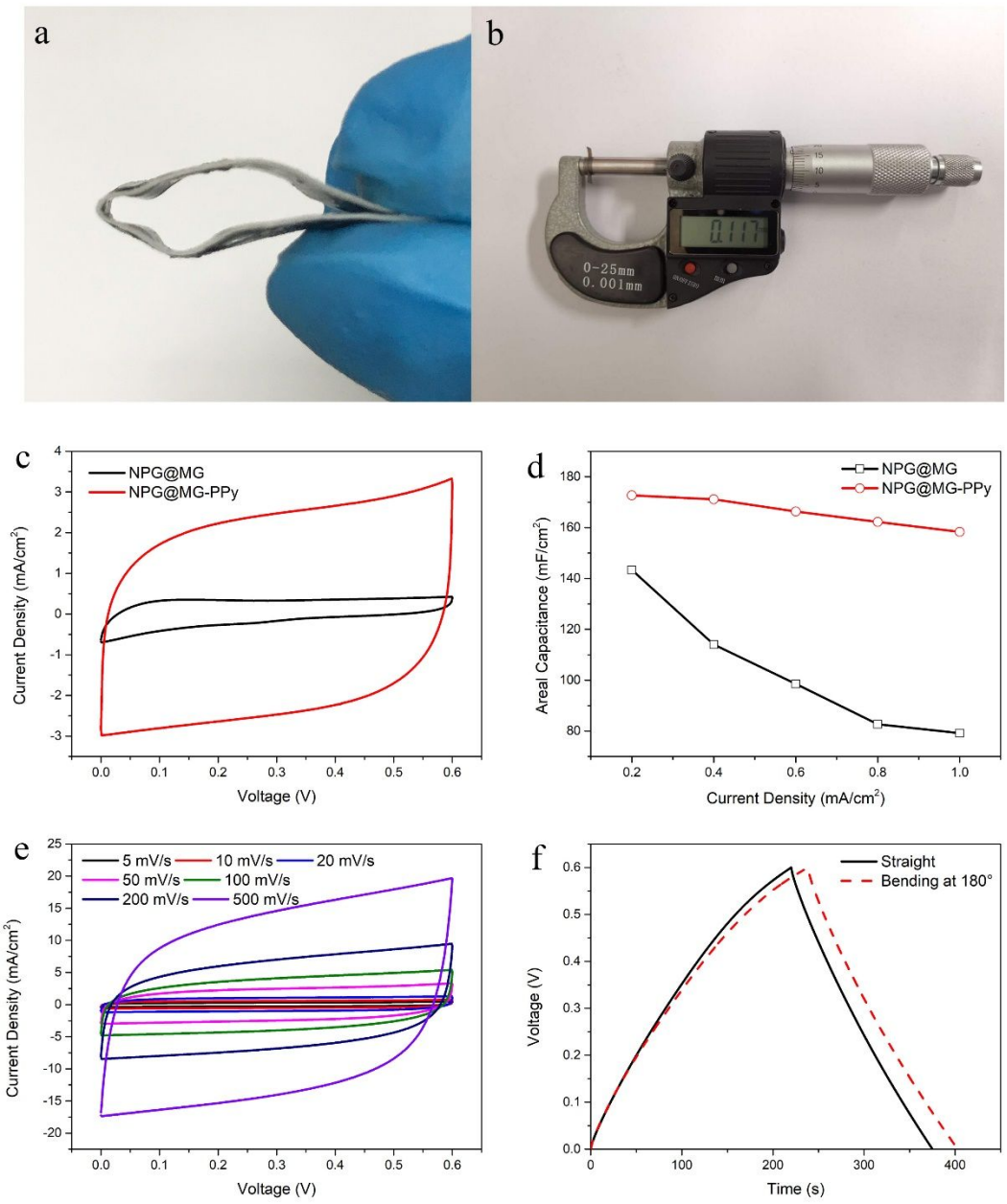


**Fig. 5** (a) Optical image of the symmetric solid-sate flexible supercapacitor based on the NPG@MG-PPy40s freestanding electrode. (b) Thickness of the as-prepared solid-state supercapacitor. (c) CV curves of the as-prepared solid-state supercapacitors at a scan rate of 5 mV/s. (d) Specific capacitance of the solid-state supercapacitors as functions of various specific current density. (e) CV and (f) galvanostatic charging/discharging curves under straight and 180° bending states of NPG@MG-PPy40s supercapacitor.

Furthermore, the Ragone plot correlating the areal energy densities (E) with areal power densities (P) demonstrated the high energy density of 9 μWh $cm^{-2}$ at the power density of 1 mW $cm^{-2}$, which surpassed many polymer film-based devices (Fig. S7c). After a comparative quantification investigation, it is equivalent to 53 times that of graphene (0.17 μWh $cm^{-2}$), 10 times that of PANI/stainless steel (0.95 μWh $cm^{-2}$) and 2 times that of PANI-ZIF-CC (4.4 μWh $cm^{-2}$). further revealing the excellent performance of NPG@MG-$PPy_{40s}$ electrode based all-solid-state supercapacitors (Table S1). Although surface NPG morphology could only provide limited capacitance, the enhanced reversibility and stability did not come from the NPG structure alone but primarily attributed to the synergistic effect of the NPG and deposited PPy film. Due to the high flexibility of MG interlayer and the PPy film as protective layer wrapping around the crystallized NPG structure, the device still exhibited stable capacitance under heavily bent condition, which is in agreement with the observation that the strain induced enhanced capacitances (Fig. 5f).

In order to satisfy the requirements of future application of implantable and portable electronics, long lifespan with good flexibility of energy storage devices is indispensable. The cyclic performance measured at a rate of 1 mA $cm^{-2}$ under relaxed states was studied (Fig. 6a). No decay in capacitance was observed, indicating the excellent cyclic stability of the fabricated all-solid-state supercapacitor. And interestingly, the enhancement in capacitance was observed after 4000 charging and discharging cycles. It was reported that the cycling stability of most previously PPy film supercapacitors were poor attributed to structural breakdown induced by repetitive large volume expansion and contraction during charging and discharging, respectively. [25,41,42] A more than 50% capacity reduction

was observed for PPy-based electrodes after 1000 cycles, while almost perfect capacitance retention was observed for the solid-state supercapacitor under relaxed state in this study. In addition, the charge/discharge curves remained linear after 8000 cycles (Fig. 6b), demonstrating the capacitive behavior of the device with less Faradic reaction. The flexible energy storage device should be able to withstand different deformation modes without mechanical failure or obvious change during electro-chemical performance. The capacitance retention of the supercapacitor with NPG@MG-$PPy_{40s}$ electrode under different bending conditions was shown in Fig. 6c-e. The insets displayed the photographs of the entire supercapacitor of 0.2 cm width while bending at angles of 0º, 90º, and 180º, respectively. The capacitance remained stable as shown in the GCD curves of the device even at extreme bending state of 180°. Besides, the voltage drops ($U_{drop}$), defined as the instantaneous drop of voltage from the top points of the curves, remained as 0.07 V at different bending angles. It indicated that the device had stable and reproducible energy storage performance.

Fig. 6f exhibits the cycling stability of the supercapacitor under repeated bending operation to simulate the real usage scenarios of portable electronics. Under such an extreme bending condition, the capacitance retention still reached almost 100 % after 300 cycles. It is indicated the excellent mechanical robustness and flexibility of the all-solid-state supercapacitor when there was no obvious reduction observed in the coulombic efficient and capacitance under different bending conditions. It was worth mentioning that such dynamic demonstration had rarely been reported, since most bending tests on flexible supercapacitors were conducted under a fixed bending angel in a static situation, because

the minor dynamical stress or strain gave arise to deviations in electrochemical curves.

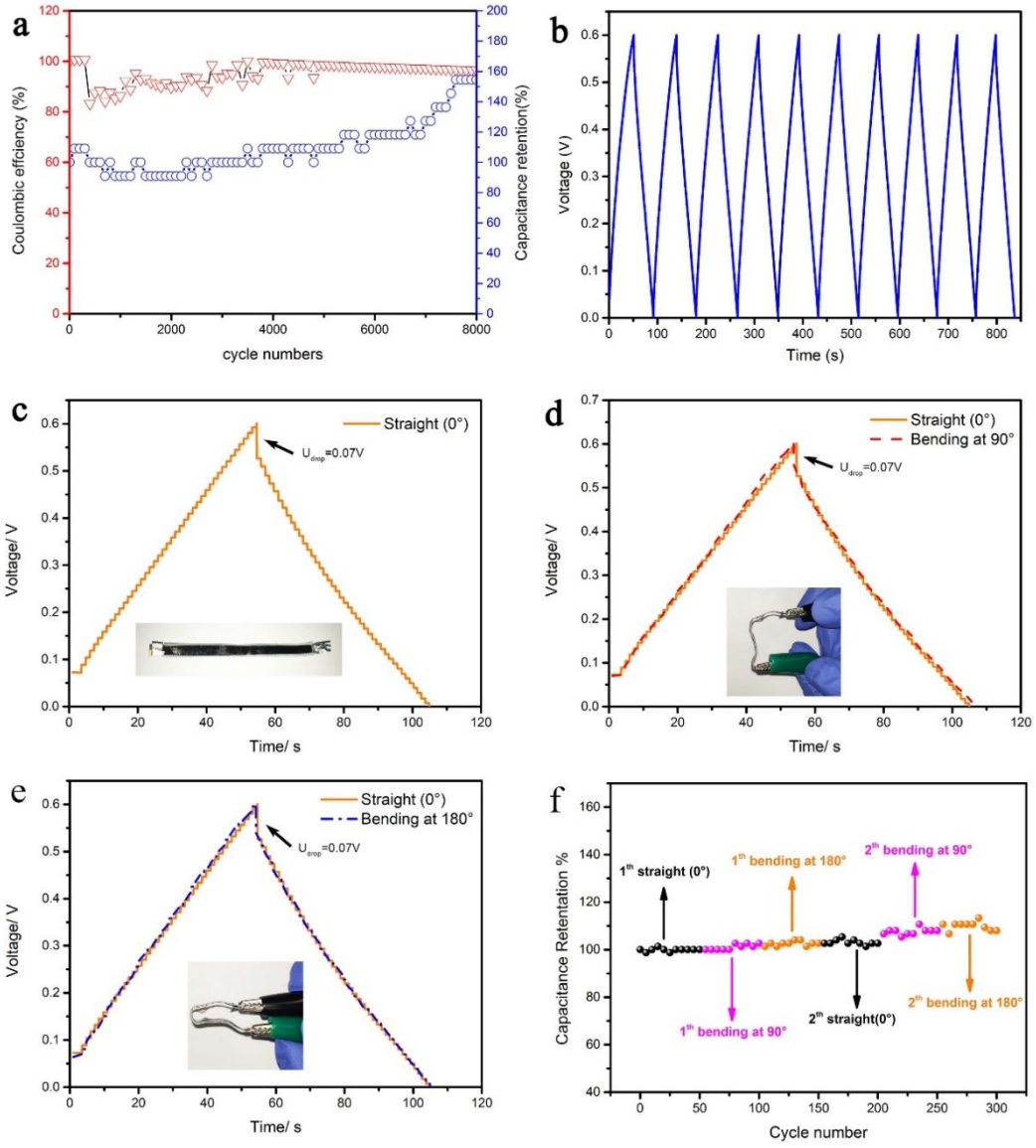


**Fig. 6** (a) Cycling performance of the solid-state supercapacitor using NPG@MG-PPy$_{40s}$ as electrode at a current density of 1 mA cm$^{-2}$. (b) Typical galvanostatic charge/discharge curves of the solid-state supercapacitor at 1 mA cm$^{-2}$. (c-e) GCD curve of the solid-state supercapacitor measured at the bending angle of 0°, 90° and 180◦, respectively. (f) Capacitance retentions of the solid-state supercapacitor under various bending states. All the above electrochemical curves were obtained at acurrent density of 0.6 mA cm$^{-2}$.

In order to further evaluate and quantify the mechanical durability, as-prepared all-solid-state supercapacitor was sustained to everlasting long-term cyclic bending with angle at 180º. The insets in Fig. 7a shows the photographs of the entire device reducing to 0.12 cm width at relaxed and different bending states. The capacitance retention still remained at almost 100% after 100 bending cycles. Fig. 7b exhibits the GCD curves of initial state compared with the state after bending 10 times. No obvious change was observed in the curves and the voltage drop ($U_{drop}$) still remained as 0.11 V. However, the retention enhancement was observed after bending 500 times. It was found that voltage drop notably decreased from 0.12V to 0.03V shown in the GCD curves (Fig. 7c-d). It indicated that the internal resistance decreases remarkably, which is in agreement with the observations of the discharge time increase and absence of capacitance decay after bending 1000 times as shown in Fig. 7e and 7a. The supercapacitor was further evaluated for stability under twisted conditions and its GCD curves are shown in Fig. 7f. Impressively, the capacitance retention still kept at 100% when the device was wrapped four laps around the tube. The excellent mechanical durability of the electrode allowed wide applications in flexible supercapacitors. It was clear that our flexible NPG@MG-$PPy_{40s}$ supercapacitor possessed superb cycling stability, excellent capacitance, high-rate capability and great flexibility.

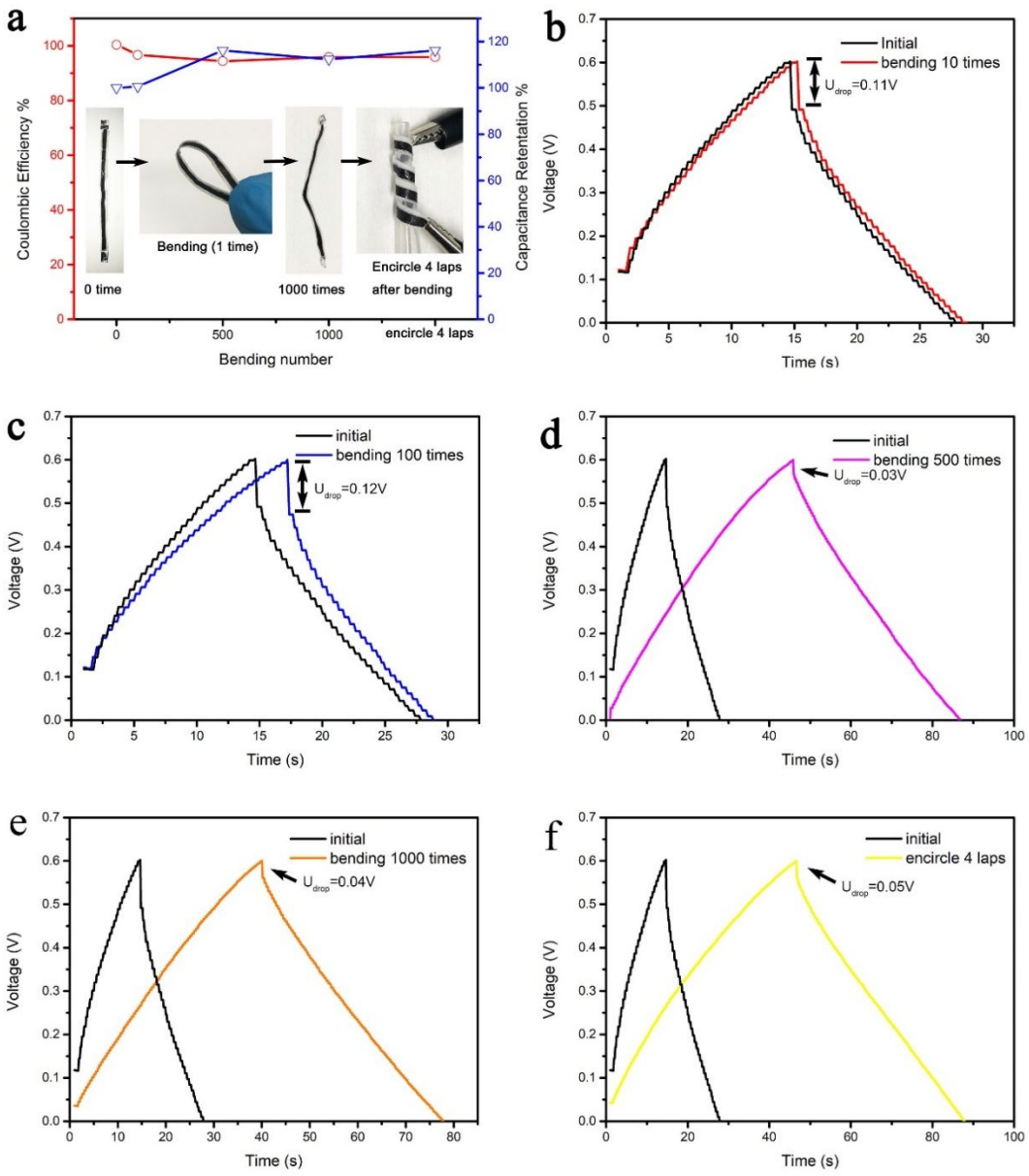


**Fig. 7** (a) Cycling performance of the solid-state supercapacitor using NPG@MG-PPy40s as electrode measured at various bending cycles and twisting deformation state. (b)-(e) GCD curves of the supercapacitor measured while it being bending after 10, 100, 500 and 1000 times, respectively. (f) GCD curve of the solid-state supercapacitor measured while it being encircling 4 laps on the tube. All the above electrochemical curves were obtained at a current density of 1 mA $cm^{-2}$.

Generally, the capacitance performance of PPy-based supercapacitor experienced a

further reduction after 5000 cycles due to the structural instability of conducting-polymer as electrode, or resulted from the structural fracture of PVA/$H_3PO_4$ solid electrolyte during deformations. However, our flexible NPG@MG-$PPy_{40s}$ electrode based supercapacitor exhibited an excellent cycling stability even in severely deformed states.

The unexpected capacitance enhancements after repeated bending observed in cyclic performance can be explained as follows:

(a) Metallic glass ribbon possesses excellent mechanical flexibility due to the amorphous state without grain boundary. The hardness and indentation modulus of the sample in MG interlayer, measured by nanoindentation test, are 5.7GPa and 103.23GPa respectively, which both are proximately 1.5 times greater than Ti-based alloy. (Supplementary Table S2).

(b) Fig. 8a-b shows the pore size at the top region of 'cone shaped protrusion' was larger than that of the bottom region. The bottom area (Fig. S1) showed strong connection between MG interlayer and ligaments, which provided pathways for charge carriers. It was assumed that the interplay of bigger space between ligaments and surface protrusion might release the internal stress when the metallic glass ribbon was under a bending state. Fig. 8c-ii illustrates the upper tensile zone and lower compressive zone when the object was in a bent state. The bumps and wrinkles of deposited PPy onto cone-shaped protrusion may be stretch and accommodates large volumetric deformation. This may also be conducive to the observed capacitance enhancement.

(c) The strain might give arise to a molecular ordering of PPy along the tension and compression directions, which could enhance ionic and electronic conductivities of PPy.

[7] This phenomenon was verified by the decreased voltage drop indicated in Fig. 7c-d as well as EIS results demonstrated in Fig. S6d.

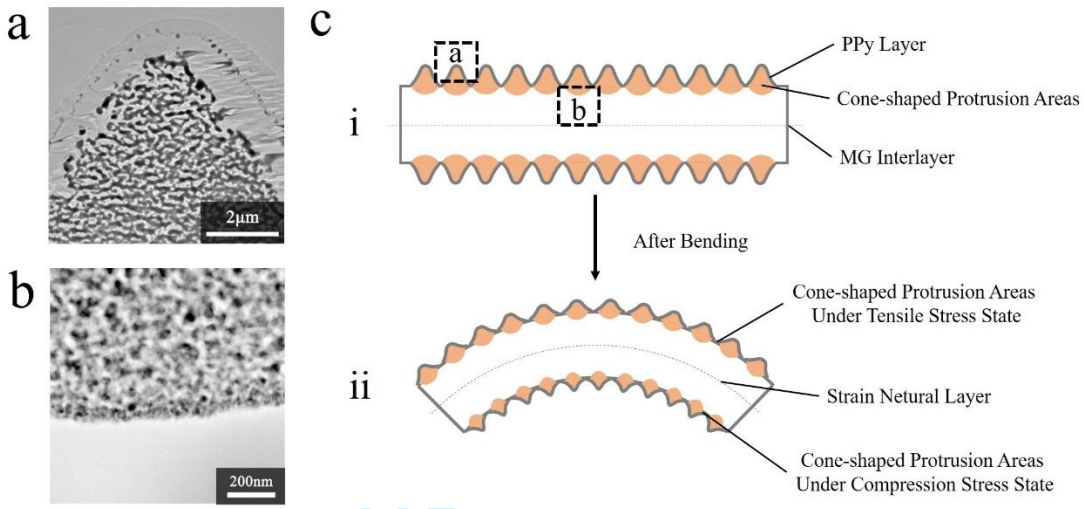


**Fig. 8** SEM image of wrinkled topology formed by specific 'cone shaped protrusion' located at (a) top region and (b) bottom region. Schematic illustration of wrinkled topology formed by specific 'cone shaped protrusion' under (i) relaxed state and (ii) bending condition.

## 3. Conclusions

To sum, we offered a facile and low-cost method to fabricate flexible composite electrode through combination of dealloyed ductile $Au_{55}Cu_{25}Si_{20}$ MG ribbons and an electrochemically polymerized PPy on surface of the resulting nanoporous gold structure. The Au-based MG ribbon was a promising current collector and the strong connection between the nanoscale ligaments and ductile MG middle layer provides pathway for electron transfer, which facilitated the pseudocapacitive process. Owing to the enhanced electrical performance and mechanical flexibility of the freestanding NPG@MG-$PPy_{40s}$ ribbon as electrode, the fabricated ultra-thin flexible all-solid-state supercapacitor exhibited high capacitances of 172 mF $cm^{-2}$ (14.8 F $cm^{-3}$), superb cycling stability and excellent

flexibility under the bending and twisting deformations. The capacitance retention was kept almost 100% after 8000 charging/discharging cycles, and even exhibited a 16.2% increase after 1000 bending cycles. This unexpected property enhancement can be attributed to the structural stability enhancement by the specific 'cone shaped areas' morphology, which might protect the PPy layer from fracture deformation. In this work, we reported a new way to design and fabricate 3D nanoporous materials integrated with conducting polymer for supercapacitor applications in the future flexible wearable electronic product fields.

**Conflicts of interest**

There are no conflicts to declare.

**Acknowledgements**

All HAADF-STEM, and EDS mapping were supported by Centre for Advanced Research of Energy and Materials in Division of Quantum Science and Engineering, Faculty of Engineering, Hokkaido University. We acknowledge Dr. Yukun Wang and Dr. Zhuoxin Liu of Prof. Chunyi Zhi's group in City University of Hong Kong for the discussion and support of PPy deposition. This work was supported by the National Natural Science Foundation of China (No. 21905180, No. 51873108), Shenzhen Science and Technology Planning Project (No. JCYJ20200109141640095 and No. JCYJ20170817110251498) and Guangdong-Hong Kong-Macao Joint Laboratory (No. 2019B121205001).

## References

1. Simon P, Gogotsi Y, Dunn B. Where Do Batteries End and Supercapacitors Begin? Science. 2014 Mar 14;343(6176):1210–1.

2. Simon P, Gogotsi Y. Materials for electrochemical capacitors. Nat Mater. 2008 Nov;7(11):845–54.

3. Meng F, Ding Y. Sub-Micrometer-Thick All-Solid-State Supercapacitors with High Power and Energy Densities. Adv Mater. 2011;23(35):4098–102.

4. Huang Y, Hu H, Huang Y, Zhu M, Meng W, Liu C, et al. From Industrially Weavable and Knittable Highly Conductive Yarns to Large Wearable Energy Storage Textiles. ACS Nano. 2015 May 26;9(5):4766–75.

5. Huang Y, Zhu M, Huang Y, Li H, Pei Z, Xue Q, et al. A modularization approach for linear-shaped functional supercapacitors. J Mater Chem A. 2016 Mar 15;4(12):4580–6.

6. Wang L, Yang H, Liu X, Zeng R, Li M, Huang Y, et al. Constructing Hierarchical Tectorum-like α-Fe2O3/PPy Nanoarrays on Carbon Cloth for Solid-State Asymmetric Supercapacitors. Angew Chem Int Ed. 2017;56(4):1105–10.

7. Zhang Z, Liao M, Lou H, Hu Y, Sun X, Peng H. Conjugated Polymers for Flexible Energy Harvesting and Storage. Adv Mater. 2018;30(13):1704261.

8. Ding Y, Kim Y-J, Erlebacher J. Nanoporous Gold Leaf: "Ancient Technology"/Advanced Material. Adv Mater. 2004;16(21):1897–900.

9. Erlebacher J, Aziz MJ, Karma A, Dimitrov N, Sieradzki K. Evolution of nanoporosity in dealloying. Nature. 2001 Mar;410(6827):450–3.

10. Fujita T, Guan P, McKenna K, Lang X, Hirata A, Zhang L, et al. Atomic origins of the high catalytic activity of nanoporous gold. Nat Mater. 2012 Sep;11(9):775–80.

11. Wang Z, Ning S, Liu P, Ding Y, Hirata A, Fujita T, et al. Tuning Surface Structure of 3D Nanoporous Gold by Surfactant-Free Electrochemical Potential Cycling. Adv Mater. 2017;29(41):1703601.

12. Qin C, Zheng D, Hu Q, Zhang X, Wang Z, Li Y, et al. Flexible integrated metallic glass-based sandwich electrodes for high-performance wearable all-solid-state supercapacitors. Appl Mater Today. 2020 Jun 1;19:100539.

13. Yao A, Yang H, Wang J-Q, Xu W, Huo J, Li R-W, et al. Flexible supercapacitor electrodes fabricated by dealloying nanocrystallized Al-Ni-Co-Y-Cu metallic glasses. J Alloys Compd. 2019 Jan 25;772:164–72.

14. Lang X, Hirata A, Fujita T, Chen M. Nanoporous metal/oxide hybrid electrodes for electrochemical supercapacitors. Nat Nanotechnol. 2011 Apr;6(4):232–6.

15. Fan Z, Yan J, Wei T, Zhi L, Ning G, Li T, et al. Asymmetric Supercapacitors Based on Graphene/MnO2 and Activated Carbon Nanofiber Electrodes with High Power and Energy Density. Adv Funct Mater. 2011;21(12):2366–75.

16. He Y, Chen W, Li X, Zhang Z, Fu J, Zhao C, et al. Freestanding Three-Dimensional Graphene/MnO2 Composite Networks As Ultralight and Flexible Supercapacitor Electrodes. ACS Nano. 2013 Jan 22;7(1):174–82.

17. Huang Y, Huang Y, Zhu M, Meng W, Pei Z, Liu C, et al. Magnetic-Assisted, Self-Healable, Yarn-Based Supercapacitor. ACS Nano. 2015 Jun 23;9(6):6242–51.

18. Yao H-L, Gao S-S, Fu Z-Q, Bao W-C, Cui Z-H, Li Y-Q, et al. Encapsulating manganese oxide nanoparticles within conducting polypyrrole via in situ redox reaction and oxidative polymerization for long-life lithium-ion batteries. Rare Met. 2021 Sep 1;40(9):2415–23.

19. Feng X, Huang Y, Li C, Chen X, Zhou S, Gao X, et al. Controllable synthesis of porous NiCo2O4/NiO/Co3O4 nanoflowers for asymmetric all-solid-state supercapacitors. Chem Eng J. 2019 Jul 15;368:51–60.

20. Kim S-I, Lee J-S, Ahn H-J, Song H-K, Jang J-H. Facile Route to an Efficient NiO Supercapacitor with a Three-Dimensional Nanonetwork Morphology. ACS Appl Mater Interfaces. 2013 Mar 13;5(5):1596–603.

21. Li H, Li X, Liang J, Chen Y. Hydrous RuO2-Decorated MXene Coordinating with Silver Nanowire Inks Enabling Fully Printed Micro-Supercapacitors with Extraordinary Volumetric Performance. Adv Energy Mater. 2019;9(15):1803987.

22. Liu Y-H, Xu J-L, Gao X, Sun Y-L, Lv J-J, Shen S, et al. Freestanding transparent metallic network based ultrathin, foldable and designable supercapacitors. Energy Environ Sci. 2017 Dec 6;10(12):2534–43.

23. Jiang S-H, Ding J, Wang R-H, Chen F-Y, Sun J, Deng Y-X, et al. Solvothermal-induced construction of ultra-tiny Fe2O3 nanoparticles/graphene hydrogels as binder-free high-capacitance anode for supercapacitors. Rare Met. 2021 Dec 1;40(12):3520–30.

24. Ning W-W, Chen L-B, Wei W-F, Chen Y-J, Zhang X-Y. NiCoO2/NiCoP@Ni nanowire arrays: tunable composition and unique structure design for high-performance winding asymmetric hybrid supercapacitors. Rare Met. 2020 Sep 1;39(9):1034–44.

25. Yuan H, Wang G, Zhao Y, Liu Y, Wu Y, Zhang Y. A stretchable, asymmetric, coaxial fiber-shaped supercapacitor for wearable electronics. Nano Res. 2020 Jun 1;13(6):1686–92.

26. Wu C, Zhang Z, Chen Z, Jiang Z, Li H, Cao H, et al. Rational design of novel ultra-small amorphous Fe2O3 nanodots/graphene heterostructures for all-solid-state asymmetric supercapacitors. Nano Res. 2021 Apr 1;14(4):953–60.

27. Huang Y, Tao J, Meng W, Zhu M, Huang Y, Fu Y, et al. Super-high rate stretchable polypyrrole-based supercapacitors with excellent cycling stability. Nano Energy. 2015 Jan 1;11:518–25.

28. Huang Y, Zhong M, Huang Y, Zhu M, Pei Z, Wang Z, et al. A self-healable and highly stretchable supercapacitor based on a dual crosslinked polyelectrolyte. Nat Commun. 2015 Dec 22;6(1):10310.

29. Huang Y, Zhu M, Pei Z, Xue Q, Huang Y, Zhi C. A shape memory supercapacitor and its application in smart energy storage textiles. J Mater Chem A. 2016 Jan 20;4(4):1290–7.

30. Jiang K, Baburin IA, Han P, Yang C, Fu X, Yao Y, et al. Interfacial Approach toward Benzene-Bridged Polypyrrole Film–Based Micro-Supercapacitors with Ultrahigh Volumetric Power Density. Adv Funct Mater. 2020;30(7):1908243.

31. Sun J, Huang Y, Fu C, Wang Z, Huang Y, Zhu M, et al. High-performance stretchable yarn supercapacitor based on PPy@CNTs@urethane elastic fiber core spun yarn. Nano Energy. 2016 Sep 1;27:230–7.

32. Liu N, Ma W, Tao J, Zhang X, Su J, Li L, et al. Cable-Type Supercapacitors of Three-Dimensional Cotton Thread Based Multi-Grade Nanostructures for Wearable Energy Storage. Adv Mater. 2013;25(35):4925–31.

33. Dong G, Fan H, Fu K, Ma L, Zhang S, Zhang M, et al. The evaluation of super-capacitive performance of novel g-C3N4/PPy nanocomposite electrode material with sandwich-like structure. Compos Part B Eng. 2019 Apr 1;162:369–77.

34. Tian W, Mao X, Brown P, Rutledge GC, Hatton TA. Electrochemically Nanostructured Polyvinylferrocene/Polypyrrole Hybrids with Synergy for Energy Storage. Adv Funct Mater. 2015;25(30):4803–13.

35. Boota M, Anasori B, Voigt C, Zhao M-Q, Barsoum MW, Gogotsi Y. Pseudocapacitive Electrodes Produced by Oxidant-Free Polymerization of Pyrrole between the Layers of 2D Titanium Carbide (MXene). Adv Mater. 2016;28(7):1517–22.

36. Zhu M, Huang Y, Deng Q, Zhou J, Pei Z, Xue Q, et al. Highly Flexible, Freestanding Supercapacitor Electrode with Enhanced Performance Obtained by Hybridizing Polypyrrole Chains with MXene. Adv Energy Mater. 2016;6(21):1600969.

37. Liu T, Finn L, Yu M, Wang H, Zhai T, Lu X, et al. Polyaniline and Polypyrrole Pseudocapacitor Electrodes with Excellent Cycling Stability. Nano Lett. 2014 May 14;14(5):2522–7.

38. Song Y, Liu T-Y, Xu X-X, Feng D-Y, Li Y, Liu X-X. Pushing the Cycling Stability Limit of Polypyrrole for Supercapacitors. Adv Funct Mater. 2015;25(29):4626–32.

39. Otero TF, Alfaro M, Martinez V, Perez MA, Martinez JG. Biomimetic Structural Electrochemistry from Conducting Polymers: Processes, Charges, and Energies. Coulovoltammetric Results from Films on Metals Revisited. Adv Funct Mater. 2013;23(31):3929–40.

40. Huang Y, Zhu M, Pei Z, Huang Y, Geng H, Zhi C. Extremely Stable Polypyrrole Achieved via Molecular Ordering for Highly Flexible Supercapacitors. ACS Appl Mater Interfaces. 2016 Jan 27;8(3):2435–40.

41. Huang Y, Li H, Wang Z, Zhu M, Pei Z, Xue Q, et al. Nanostructured Polypyrrole as a flexible electrode material of supercapacitor. Nano Energy. 2016 Apr 1;22:422–38.

**Highly flexible, mechanically strengthened metallic glass-based supercapacitor electrode with enhanced capacitance and cyclic stability**

Yi Xu[a,b], Pak Man Yiu[d], Yu-Kun Wang[d], Xiao-Meng Qin[d], Tamaki Shibayama[e], Seiichi Watanabe[e], Masato Ohnuma[e], Da-Zhu Chen[a], Hua Cheng[c], Chan-Hung Shek*[d], Zhouguang Lu*[c], Chen Liu*[a]

a. Guangdong Research Center for Interfacial Engineering of Functional Materials, College of Materials Science and Engineering, Shenzhen University, Shenzhen 518060, PR China

b. College of Physics and Optoelectronic Engineering, Shenzhen University, Shenzhen.

c. Guangdong-Hong Kong-Macao Joint Laboratory for Photonic-Thermal-Electrical Energy Materials and Devices, Department of Materials Science and Engineering, Southern University of Science and Technology, Shenzhen 518060, PR China

d. Department of Materials Science and Engineering, City University of Hong Kong, No.83 Tat Chee Avenue, Kowloon Tang, Hong Kong, China

e. Centre for Advanced Research of Energy and Materials, Division of Quantum Science and Engineering, Faculty of Engineering, Hokkaido University, Kita 13, Nishi 8, Kita Ku, Sapporo 0608628, Japan

* Email address: liuchen@szu.edu.cn (C. Liu), luzg@sustech.edu.cn (Z. G. Lu), apchshek@cityu.edu.hk (C.H.Shek)

## Experimental Section

**Nanoporous gold (NPG) preparation** Free-standing NPG ribbon with MG interlayer was fabricated by chemically dealloying $Au_{55}Cu_{25}Si_{20}$ metallic glass ribbon. Au-based MG ribbon of approximately 50μm thickness was cleaned by acetone solution. After cleaning, the MG ribbon was immersed into freshly prepared $FeCl_3$(0.1 mol) in HCl solution (Sigma-Aldrich). The density and thickness of cone-shaped protrusion areas could be controlled by adjusting the dealloying preparation conditions. In order to show the optimum performance, the dealloying time and temperature were set as 20min and 70 ℃ respectively. Then, the 30 mL $FeCl_3$ in a 50 mL tricollar flask containing MG ribbon was heated up to 70℃ by heating mantle. After dealloying for 20min, only copper was dissolved selectively from the metallic glass ribbon. The as-prepared NPG ribbons were carefully rinsed with deionized water (18.2 MΩ.cm) to remove the residual iron chloride solution.

**Fabrication of NPG@MG-PPy electrode, and NPG@MG-$PPy_{40s}$ electrode into All-Solid-State Supercapacitors** The as-prepared NPG@MG ribbon were first cleaned in 50 mL acetone. Then, the PPy was electrochemical polymerized under constant voltage of 0.8 V versus Ag/AgCl onto the surface of freestanding NPG ribbon with MG interlayer using the aqueous solution containing p-toluenesulfonic acid (0.1 m), sodium p-toluenesulfonic (0.3 m), and pyrrole monomer (300 μL) for 10 s, 20 s, 40 s and 60 s, which is denoted as NPG@MG-$PPy_{10s}$, NPG@MG-$PPy_{20s}$, NPG@MG-$PPy_{40s}$ and NPG@MG-$PPy_{60s}$, respectively.

Two identical as-prepared NPG@MG-$PPy_{40s}$ electrodes were assembled together with a gel electrolyte. The electrolyte consisting of 6 g $H_3PO_4$ and 6 g PVA powders were

added to 60 mL deionized water. Subsequently, the mixture was heated to 90 °C under stirring until the mixture becomes clear. The solid-state supercapacitor was obtained after the electrolyte solidification at room temperature.

**Electrochemical Tests and Structural Characterizations** Scanning electron microscopy (SEM) images were obtained with a JSM 6335F FE-SEM (JEOL) operating at 5 kV, Energy-dispersive X-ray spectroscopy (EDS) was recorded at 20 kV. For examining the cross-section of 'cone shaped protrusion' regions, TEM samples were obtained with JEM-9320 Focused Ion Beam (FIB) system. HRTEM images were taken with a JEM-2100F (JEOL) transmission electron microscope operated at 200 kV. HAADF-STEM images and elemental mapping was acquired with a Titan G2 60-300 (FEI) spherical aberration corrected Scanning Transmission Electron Microscope. The crystallographic characteristics of the samples were characterized by powder X-ray diffraction (Rigaku Smartlab) using Cu Kα radiation with a 2θ angle ranging from 10 to 90. Electrochemical measurements were carried out on an electrochemical workstation (CHI760C). Cycle tests were conducted by a Land 2001A battery testing system.

Specific capacitances of supercapacitors were calculated from GCD curves at different current densities using the equations(1) and (2) below,

$$C_a = \frac{I \times \Delta t}{\Delta V \times A} \qquad (1)$$

$$C_v = \frac{I \times \Delta t}{\Delta V \times V} \qquad (2)$$

where $C_A$ (mF cm$^{-2}$) is the areal specific capacitance, Cv (mF cm$^{-3}$) is the volumetric specific capacitance, I (mA) is the discharge current, Δt (s) is the discharge time, A (cm$^{-2}$) is the effective area of electrodes, V(cm$^{-3}$) is the total volume of the whole device, and ΔV

(V) is the operating voltage (determined from the discharge curves excluding potential drop). The volumetric energy densities and power densities were calculated by using the following equations(3) and (4):

$$E_a = \frac{C_a \times \Delta V^2}{2 \times 3600} \quad (3)$$

$$P_a = \frac{E_a}{t} \times 3600 \quad (4)$$

where $E_a$ (mWh cm$^{-2}$) is the areal energy density, $C_a$ (mF cm$^{-2}$) is the areal specific capacitance, ΔV (V) is the operating voltage excluding potential drop, $P_a$ (mW cm$^{-2}$) is the areal power density, t (s) is discharging time.

**Modulus calculation for nanoindentation experiment** Nanoindentation experiments have been performed employing a MTS RT/30 Electro-Mechanical Material Testing System with a Berkovich indenter. More than 30 indentation tests have been conducted randomly at the surface of the sample by applying the same indentation testing conditions. The maximum indentation depth reached by the indenter was fixed at 2000 nm.

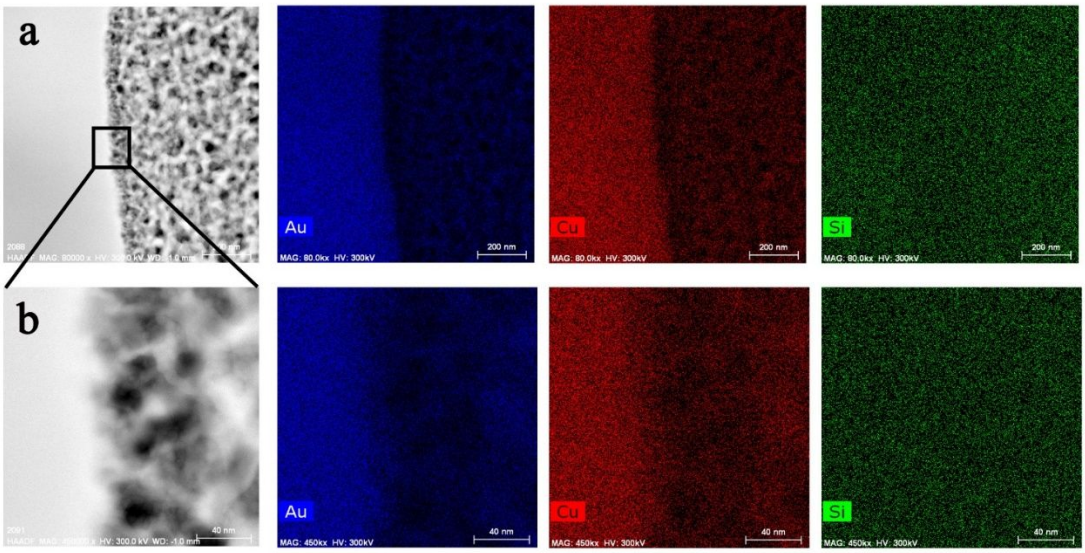


**Figure S1** (a) HAADF-STEM images of bottom region of cone shape protrusion areas and EDS elemental mapping of Au, Cu and Si. (b) Enlarged image in selected area and EDS elemental mapping of Au, Cu and Si.

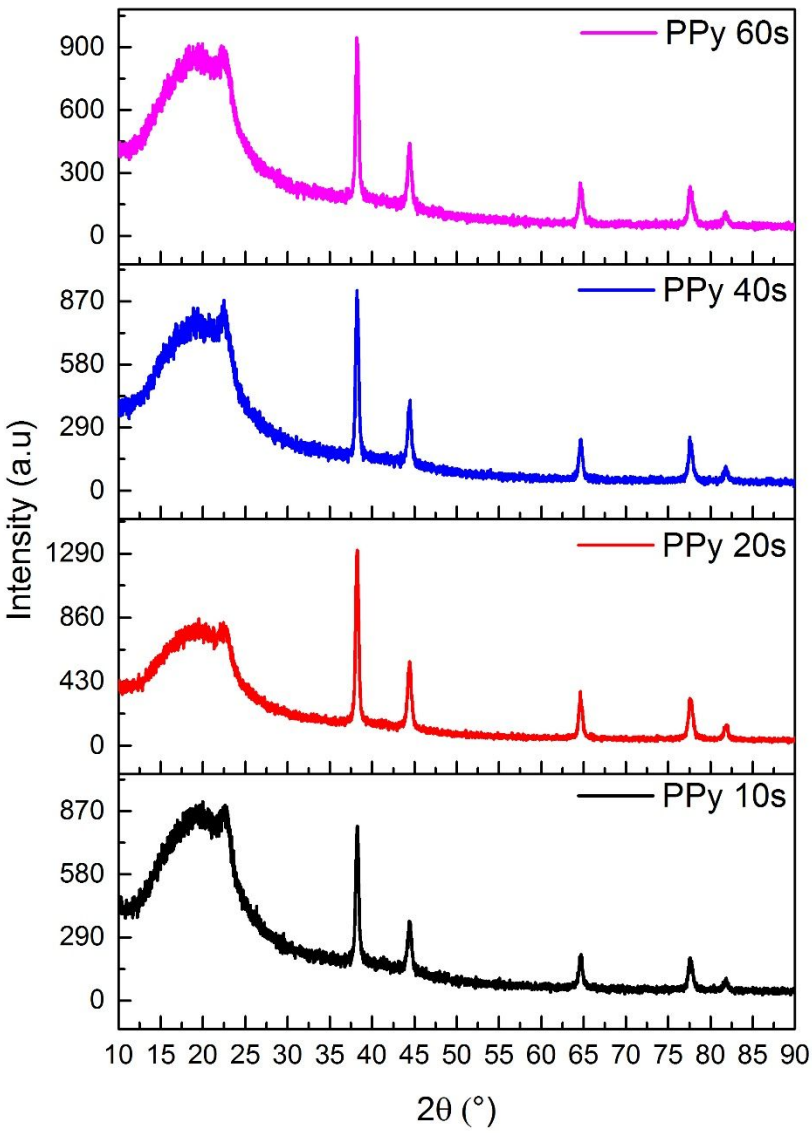


**Figure S2** XRD patterns of NPG@MG and PPy membrane formed using different PPy electrochemical polymerization times.

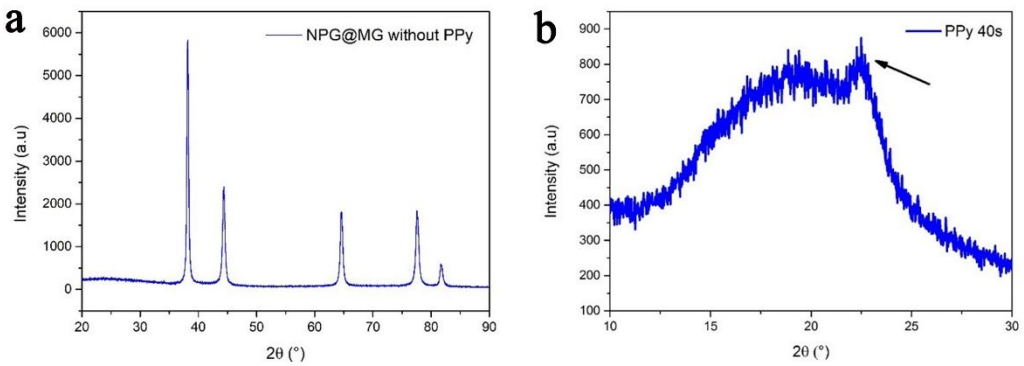


**Figure S3** (a) XRD pattern of NPG@MG without PPy deposition. (b) Magnified XRD patterns (10°–30°) of NPG@MG and PPy membrane (electrochemical polymerization time = 40 s).

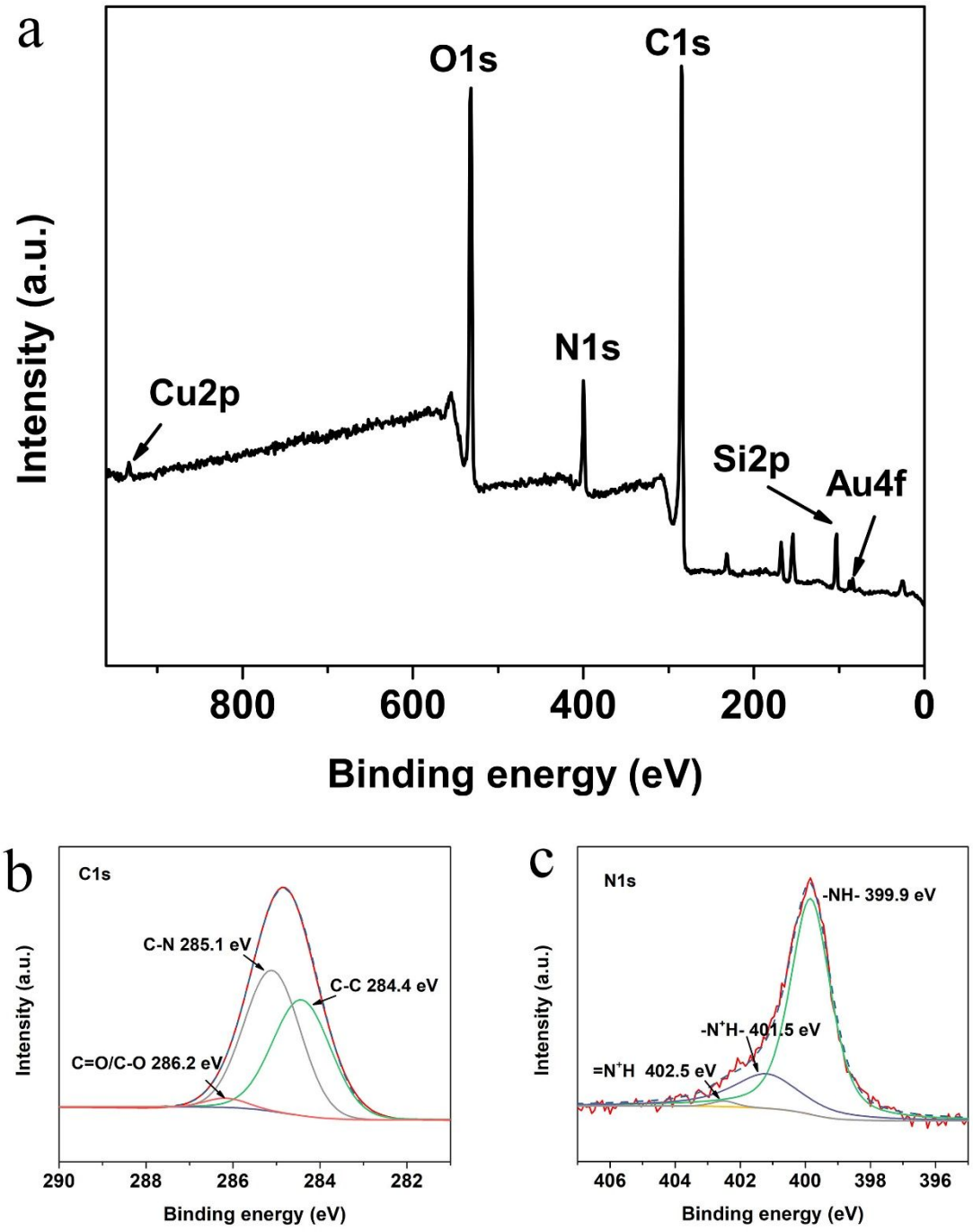


**Figure S4** (a) XPS full spectra; (b) C1s core level and (b) N1s core level of the NPG@MG-PPy composite film.

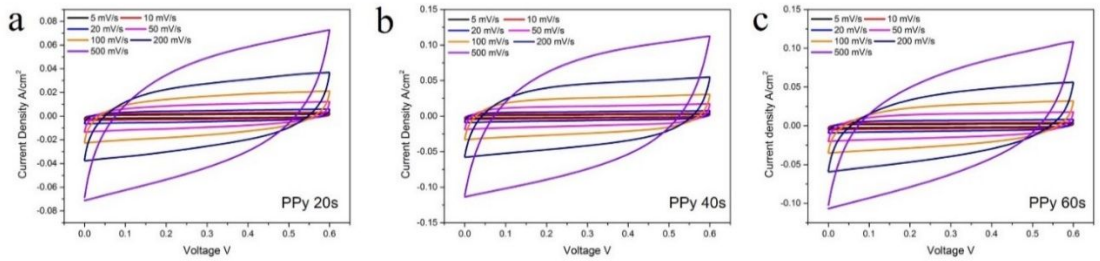


**Figure S5** CV curves of the $PPy_{20s}$, $PPy_{40s}$ and $PPy_{60s}$ membrane deposited on NPG morphology at different scan rates.

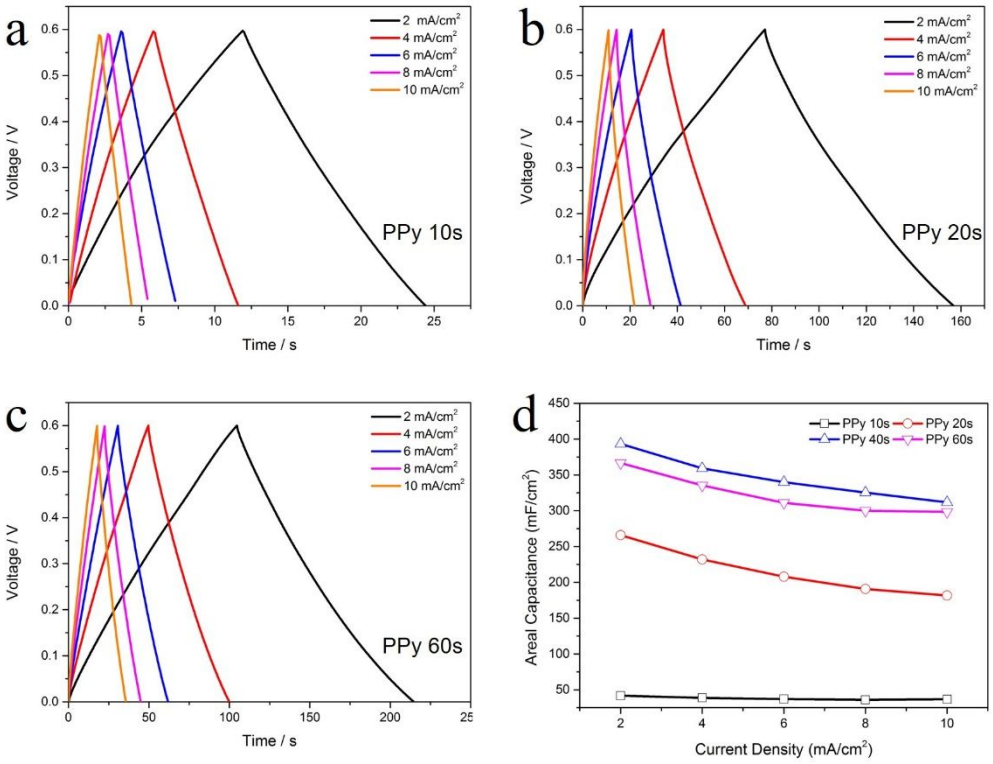


**Figure S6** Galvanostatic charging/ discharging curves of the (a)NPG@MG-$PPy_{10s}$ (b) NPG@MG-$PPy_{20s}$ (c) NPG@MG-$PPy_{60s}$ as electrode at different current densities. (d) Specific capacitances as functions of various current densities.

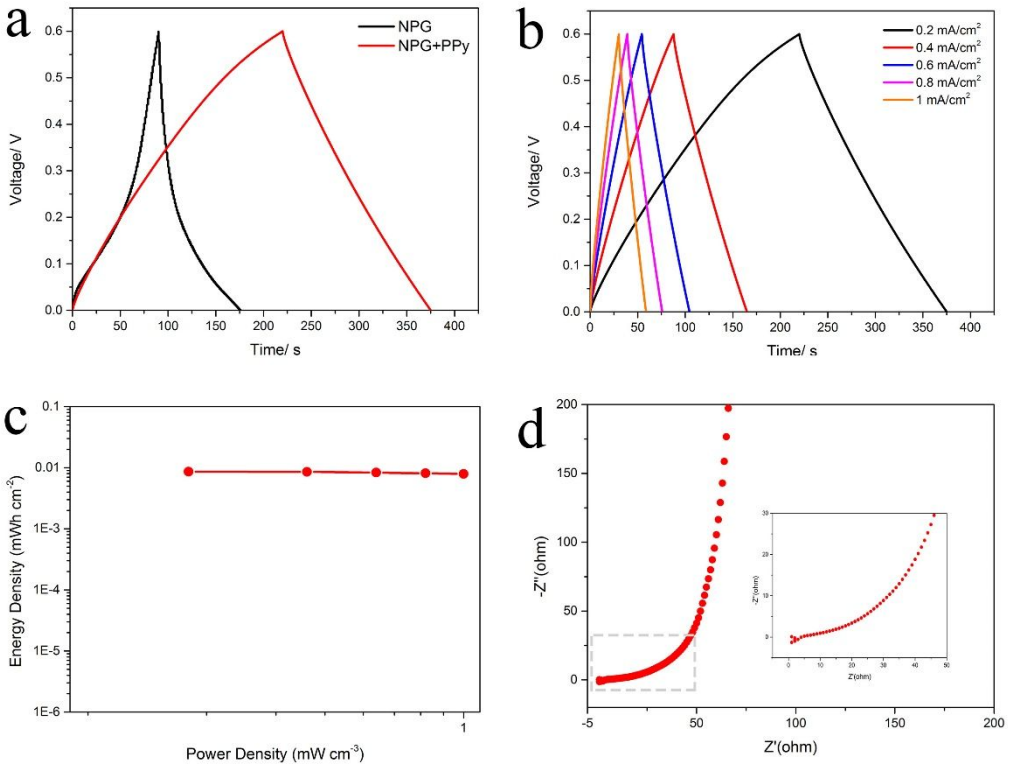


**Figure S7** (a) Galvanostatic charging/ discharging curves of the as-prepared solid-state supercapacitors using NPG and NPG@MG-$PPy_{40s}$ as electrodes. (b) Galvanostatic charging/ discharging curves and (c) ragone plot of the solid-state supercapacitors using NPG compared NPG@MG-$PPy_{40s}$ as electrode. (d) Nyquist plots of the NPG@MG-$PPy_{40s}$ as electrode (measured in 0.5M H2SO4 with a three electrode configuration), enlarged image in selected area.

From the Nyquist plot, a charge transfer resistance can be obtained from the diameter of the semicircle on this plot. Figure S7d demonstrate the semicircle in the plot disappears that indicates that the charge-transfer resistance decreased to nearly zero. The interconnection between PPy film and 3D nano-porous gold might provide the ion transfer path, and Au-based BMG metal matrix also could be served as good current collector.

**Table S1** Performance comparison of the NPG@MG-PPy film in all-solid-state supercapacitors with other graphene and Polymer based materials.

| Electrode Materials | Electrolyte | $C_a$ mF $cm^{-2}$ | $C_v$ F $cm^{-3}$ | $E_a$ μWh cm-2 | $E_v$ mWh cm-3 | Ref |
|---|---|---|---|---|---|---|
| NPG@MG-PPy | PVA/$H_2SO_4$ | 172 | 14.8 | 8.7 | 0.74 | This work |
| Graphene | PVA/$H_2SO_4$ | 1.7 | - | 0.17 | - | (1) |
| PANI/stainless steel | PVA/$H_2SO_4$ | 41 | - | 0.95 | - | (2) |
| PANI nanowires | PVA/$H_2SO_4$ | 45 | - | - | 0.78 | (3) |
| PANI-ZIF-CC | PVA/$H_2SO_4$ | 35 | 116 | 4.4 | 0.0161 | (4) |
| PANI/rGO | PVA/$H_2SO_4$ | 13 | 66.2 | - | 1.51 | (5) |
| Parallel cylindrical mesoporous PPy/rGO | PVA/$H_2SO_4$ | 81 | 102 | - | 2.3 | (6) |
| PPy-NPG | PVA/$HClO_4$ | 1.8 | 30 | - | 2.8 | (7) |
| PPy/l-Ti3C2 | PVA/$H_2SO_4$ | 35 | 291 | - | 10 | (8) |

Notes: $C_a$-Areal capacitance, $E_a$-Volumatic capacitance, $E_a$-Areal energy density, $E_v$-Volumatic capacitance

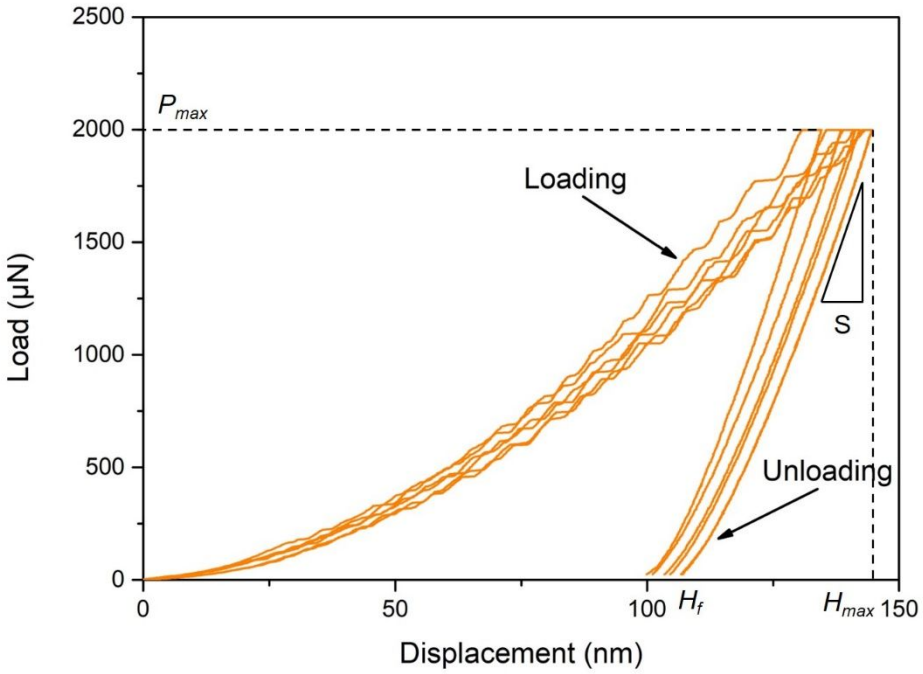


**Figure S8** The indentation load–depth curve (obtained from FE simulations) with the upper unloading curve fitted by Eq. (2)

The figure above shows the load–displacement curve measured during nanoindentation on a $Au_{55}Cu_{25}Si_{20}$ sample by a Perkovich tip. Use the Oliver–Pharr method[9] to calculate the hardness and the value of *E/(1−v2)*.

The Oliver–Pharr method begins by fitting the unloading portion of the indentation load–depth data to the power-law relation shown below:

$$P = \alpha(h - h_f)^m \qquad (1)$$

where P is load, h indentation depth, hf maximum indentation depth and the constant α and m are fitting parameters. Additionally, the upper unloading data are used to fit Eq. (1) through regression analysis when using the Oliver–Pharr method.

Once the three fitting parameters, and $Hf$ in Eq. (1) are obtained, the contact stiffness , which is defined as the slope of the unloading curve at the maximum indentation depth, can be computed from equation as follows :

$$S = \frac{d_p}{d_h}|_{h=h_m} = Bm(h_m - h_f')^{m-1} \qquad (2)$$

The contact depth of the indentation can be calculated by following the Oliver–Pharr method as :

$$h_c = h_{max} - \varepsilon\frac{P_{max}}{S} \qquad (3)$$

From the graph, $S$=69.1583 mN nm$^{-1}$; $h_{max}$=141.1 nm; $P_{max}$=1998.082 mN ,

$$H_c = 141.1 - 0.75 \times \frac{1998.082}{69.1583} = 119.43nm$$

For a perfect Berkovich indenter, the projected contact area, Ac, is a function of the contact depth, hc, and it is expressed as follows:

$$A_c = 24.56 \times {H_c}^2 = 24.56 \times (119.43)^2 = 350{,}312\ nm^2$$

The hardness and reduced modulus are obtained from the equations below:

$$H = \frac{P_{max}}{A} \qquad (4)$$

$$E_r = \frac{\sqrt{\pi}\ S}{2\beta\sqrt{A_c}} \qquad (5)$$

Therefore, the hardness $H = \frac{1998.08\ mN}{350312\ nm^2} = 5.7GPa$

$\beta$=1.034 for a Berkovich punch

$$E_r = \frac{\sqrt{\pi} \quad 69.15mN\ nm^{-1}}{2 \times 1.034\ \sqrt{350312}nm^2} = 94.64\ GPa$$

For the diamond tip, $E$=1140 GPa and $v$=0.07, and so the reduced modulus for the sample is:

$$(\frac{E}{1-v^2})_{sample} = \frac{1}{\frac{1}{94.64} - \frac{1-0.07^2}{1140}} = 103.23\ GPa$$

Compared with hardness and indentation modulus of Ti-based alloy, $Au_{55}Cu_{25}Si_{20}$ sample exhibit excellent hardness and reduced modulus.

**Table S2** Comparison of indentation hardness with indentation(reduced) modulus for $Au_{55}Cu_{25}Si_{20}$ and $Ti_{2448}$ single crystals on various surfaces

| Sample | Indentation hardness/ Gpa | Indentation modulus/ Gpa | Ref |
|---|---|---|---|
| $Au_{55}Cu_{25}Si_{20}$ | 5.7 | 103.23 | This work |
| $Ti_{2448}$(111) | 3.5 | 78.9 | [10] |

## References


1. Kou L, Huang T, Zheng B, Han Y, Zhao X, Gopalsamy K, et al. Coaxial wet-spun yarn supercapacitors for high-energy density and safe wearable electronics. Nat Commun. 2014 May 2;5(1):3754.

2. Fu Y, Wu H, Ye S, Cai X, Yu X, Hou S, et al. Integrated power fiber for energy conversion and storage. Energy Environ Sci. 2013 Feb 20;6(3):805–12.

3. Meng C, Maeng J, John SWM, Irazoqui PP. Ultrasmall Integrated 3D Micro-Supercapacitors Solve Energy Storage for Miniature Devices. Adv Energy Mater. 2014;4(7):1301269.

4. Wang L, Feng X, Ren L, Piao Q, Zhong J, Wang Y, et al. Flexible Solid-State Supercapacitor Based on a Metal–Organic Framework Interwoven by Electrochemically-Deposited PANI. J Am Chem Soc. 2015 Apr 22;137(15):4920–3.

5. Song B, Li L, Lin Z, Wu Z-K, Moon K, Wong C-P. Water-dispersible graphene/polyaniline composites for flexible micro-supercapacitors with high energy densities. Nano Energy. 2015 Sep 1;16:470–8.

6. Tian H, Qin J, Hou D, Li Q, Li C, Wu Z-S, et al. General Interfacial Self-Assembly Engineering for Patterning Two-Dimensional Polymers with Cylindrical Mesopores on Graphene. Angew Chem. 2019;131(30):10279–84.

7. Meng F, Ding Y. Sub-Micrometer-Thick All-Solid-State Supercapacitors with High Power and Energy Densities. Adv Mater. 2011;23(35):4098–102.

8. Zhu M, Huang Y, Deng Q, Zhou J, Pei Z, Xue Q, et al. Highly Flexible, Freestanding Supercapacitor Electrode with Enhanced Performance Obtained by Hybridizing Polypyrrole Chains with MXene. Adv Energy Mater. 2016;6(21):1600969.

9. Oliver WC, Pharr GM. An improved technique for determining hardness and elastic modulus using load and displacement sensing indentation experiments. J Mater Res. 1992 Jun;7(6):1564–83.

10. Zhang Y, Li S, Hao Y, Yang R. Nanoindentation study on Ti–24Nb–4Zr–8Sn single crystals. The Chinese Journal of Nonferrous Metals. 2010:S1